



## Full Text View

Volume 29, Issue 11 (November 1999)

## Journal of Physical Oceanography

Article: pp. 2851–2871 | [Abstract](#) | [PDF \(801K\)](#)

## Influences of Topography on the Modeling of Abyssal Water Masses. Part I: Effects of Channel Representation

Ross J. Murray and C. J. C. Reason

*School of Earth Sciences, University of Melbourne, Parkville, Victoria, Australia*

(Manuscript received May 29, 1998, in final form December 28, 1998)

DOI: 10.1175/1520-0485(1999)029<2851:IOTOTM>2.0.CO;2

## ABSTRACT

Connections between basins below 4000 m, which may or may not be resolved in computer-generated model topography, have been found to have a considerable impact on the movement of Antarctic Bottom Water and on deep ocean temperatures. Blocked ridges produce sharply stepped tracer distributions and a complete absence of Antarctic influence in the North Atlantic. With channels opened, mass transports through them are of the right order, but interbasin gradients are too small and the water is too dense. Because mixing processes in the channels are poorly represented, some modification of channel properties may be necessary in order to achieve realistic water property distributions. This may be done by making local adjustments of diffusive and viscous coefficients, by the use of single width channels (which may be included inadvertently or by design in topography generation and which allow diffusive and limited advective exchanges between basins), and, when vertical resolution allows it, by an appropriate choice of sill depth at the interbasin channels. The various methods work by controlling the mixing of bottom water with deep water by advection and diapycnal diffusion.

### 1. Introduction

Antarctic Bottom Water (AABW) occupies the deep ocean basins of the Atlantic and Indian Oceans below 4000 m (Tomczak and Godfrey 1994). The water filling these basins collects principally in the Atlantic–Indian–Antarctic basin and then proceeds through a number of deep basins connected by channels through fracture zones at depths characteristically 4200–4500 m. The existence of these channels allows the water mass to infiltrate basins remote from its source region without excessive dilution with North Atlantic Deep Water (NADW). The pathways of this spreading have been inferred from water property gradients, as discussed by Tomczak and Godfrey. AABW is colder and fresher than the NADW above it, but gradually becomes warmer (Fig. 1) and more saline as it spreads farther northward and mixes with the latter.

The deep basins of the Atlantic Ocean are divided northward of 50°S by the Mid-Atlantic Ridge. The main pathway for AABW in the Atlantic is via the Argentine, Brazil, and “North West Atlantic Basin” (labeled NW Atlantic Basin in Fig. 1) on the western side. These basins are connected by channels through a number of fracture zones, in which northward movement is retarded. The depths of many of the channels are now known, and Thompson (1995) has recently given a

## Table of Contents:

- [Introduction](#)
- [Model formulation](#)
- [The effects of channel](#)
- [The effects of channel](#)
- [Conclusions](#)
- [REFERENCES](#)
- [APPENDIX](#)
- [TABLES](#)
- [FIGURES](#)

## Options:

- [Create Reference](#)
- [Email this Article](#)
- [Add to MyArchive](#)
- [Search AMS Glossary](#)

## Search CrossRef for:

- [Articles Citing This Article](#)

## Search Google Scholar for:

- [Ross J. Murray](#)
- [C. J. C. Reason](#)



tracers with  $K_H = 10^6 \text{ cm}^2 \text{ s}^{-1}$ . Vertical viscosity was set to  $K_M = 20 \text{ cm}^2 \text{ s}^{-1}$  at all levels, and was not enhanced in unstable columns because this tends to produce noisy fields of vertical velocity.

Since the primary interest was the abyssal flow in the Atlantic Ocean, the horizontal grid was longitudinally compressed from  $5.625^\circ$  in the Indian and Pacific sectors to  $3^\circ$  in the Atlantic sector, with a smooth transition of grid size in the sectors  $90^\circ\text{--}45^\circ\text{W}$  and  $0^\circ\text{--}45^\circ\text{E}$ . The latitudinal resolution was  $2.5^\circ$  throughout. In order to avoid the need for Fourier filtering, which has the capacity to create unintended extrema where it is operative, the Arctic Ocean was excluded with a wall at  $75^\circ \text{N}$ , and a fairly short momentum time step of 20 minutes was used. All simulations employed a tracer time step of 2 days at the surface, with acceleration factors ([Bryan 1984](#)) increasing in the lower layers from 1 to 8.

In addition to giving a better representation of channels and flows, the enhanced resolution in the Atlantic Ocean also allows smaller values of lateral viscosity and diffusivity to be used there. These make for a sharper delineation of tracer gradients and boundary currents as well as a more vigorous circulation. Tracer mixing was horizontally oriented, with a diffusivity of  $A_H = 1 \times 10^7 \text{ cm}^2 \text{ s}^{-1}$  being used throughout. This value is in the numerically acceptable range for the Atlantic sector and in the higher latitudes, where the maximum grid dimensions do not exceed  $3^\circ$ , but is rather low for the tropical Pacific Ocean. However, no obvious signs of checkerboarding were found in this part of the Pacific, or anywhere else in the global ocean. Because the consequences of transgressing limits on viscosity are more immediate than in the case of diffusivity and in order to keep the viscosity low in the area of interest, where the higher resolution allows it, a spatially variable viscosity was used,

$$A_M = \max \left[ \beta(\phi) \left( \frac{\sqrt{3} \max(\Delta\lambda \cos\phi, \Delta\phi)}{\pi} \right)^3, \right. \\ \left. 3 \times 10^9 \text{ cm}^2 \text{ s}^{-1} \right].$$

The first term is the Munk condition, which sets the lower limit on the horizontal viscosity when the resolution is greater than about  $1^\circ$  ([Bryan et al., 1975](#)), and the second is a global minimum applied to prevent grid Reynolds violations. Spatial variation of the eddy viscosity generates extra metric terms, which are derived in the appendix.

Bottom topography was interpolated after slight smoothing of the Scripps  $1^\circ$  dataset to the degree necessary to give representative grid cell values. The interpolated topography was then modified by hand so as to resolve important channels and sills. Particular attention was paid to the connections between the abyssal basins, which occupied the bottom model level in the 12-level model. To limit the likelihood of topographical instabilities ([Killworth 1987](#)), ocean columns were deepened where necessary so that the difference in the depth of adjacent cells should not exceed a prescribed amount (usually four levels) depending on depth; unlike smoothing, this had no effect on the topography–ocean mask for the bottom level.

The model was forced annual-averaged [Hellerman and Rosenstein \(1983\)](#) wind stresses and constant tracer relaxation fields. Following [Hirst and Cai \(1994\)](#), who showed that a strong restoration to wintertime surface tracer values most closely reproduces water mass characteristics when time-invariant upper boundary conditions are employed, tracers were restored with a 4-day relaxation time constant to the 10-m climatology of [Levitus \(1982\)](#) for the winter months in each hemisphere. Also, some of the modifications to the forcing fields suggested by these authors to correct inadequacies in the Levitus data in water mass formation regions were used. Tracer values in the Greenland Sea were set to  $-1.9^\circ\text{C}$ , 34.84 psu, and salinities in the SW Ross and SW Weddell Seas were set to 34.85–34.90 and 34.80 psu, respectively. In spite of these measures, the AABW entering the deep Atlantic basins was  $0.5^\circ\text{C}$  too cold and the NADW  $2.4^\circ\text{C}$  too warm, making the density difference between the water masses  $2\frac{1}{2}$  times too large. Since the object of this project was not to study the formation and downslope flow of these waters, but rather their interaction in the abyss, an interior restoration was applied. Bottom level temperatures and salinities at points in the path of the density flow in the Irminger and Weddell Sea troughs were restored to climatology using a 50-day time constant.

Experiments were integrated to quasi equilibrium from an initial condition interpolated from the 3D Levitus annual-average ocean climatology. Rms changes in temperature in the deep ocean over the last 10 000 time steps were of the order  $0.03^\circ\text{C}$ , that is,  $2 \times 10^{-12} \text{ }^\circ\text{C s}^{-1}$ . Tendencies for a single time step were larger than this ( $\sim 2 \times 10^{-11} \text{ }^\circ\text{C s}^{-1}$ ) but still very much smaller than advection and diffusion terms ( $\sim 10^{-9} \text{ }^\circ\text{C s}^{-1}$ ).

Simulations all used the same horizontal grid and forcings, but differed in the specification of bottom-level channel topography and mixing coefficients, and vertical resolution. The details of these variations are described in the following sections.

### 3. The effects of channel topography

A number of experiments were conducted to investigate how varying the representation of fracture zones in the model topography would affect the latitudinal variation of bottom-water properties. This was done by varying the topography–

ocean masks for the 3700–4600 m layer, which roughly corresponds to the domain of AABW; the masks for levels above 3700 m were the same in all experiments. The bottom depth range is occupied by just one level in the 12-level model, and by two in the 21-level model.

The obstructions of interest are indicated in [Fig. 1](#). In all experiments, the Walvis Ridge (WR), Hunter Channel (HC), and Kane Gap (KG) were blocked at the 3700–4600 m level. The remaining passages (SST, AIR, VS, RFZ, CR, VFZ, and DG) were either blocked or resolved in a number of ways, as shown in [Fig. 2](#); in each experiment, all channels were treated in a consistent fashion. In addition, one simulation was performed in which the bottom level topography was as generated by the topographic interpolation program.

### *a. Twelve-level experiments*

Simulated temperatures in the western and eastern sides of the Atlantic Ocean are shown as meridional profiles for the 2800–3700 and 3700–4600 m layers, representing the 11th and 12th (or 3250 and 4150 m) levels in the 12-level model, used here ([Fig. 3](#)). The points chosen for averaging at each latitude are those which are ocean points at level 12 on one or other side of the Mid-Atlantic Ridge. To emphasize the changes at the basin boundaries, a few points were masked out where parts of adjoining basins occupied the same latitude row. The modeled profiles are compared to those obtained from Levitus after horizontal smoothing and interpolation to the model grid. In the Levitus traces, temperatures at both levels increase northward (except in the Angola Basin) as the waters progressively mix with the overlying NADW. The small dip at 30°S in [Fig. 3a](#) is due to the movement of the coldest water in the Argentine Basin toward the Vema Sill. Property gradients in the Levitus data are sharpened at the latitudes of the submarine ridges in data interpolated to the bottom model level (see also [Fig. 1](#)), but not in those of the level above. The profiles of salinity and density (not shown) are distinctly similar to those of temperature in both observed and modeled datasets. This reflects the adiabatic mixing of essentially just two water masses, represented by the tracer values (in both levels) at 68°S (AABW) and in level 11 at 48°N (NADW). It will therefore be in order to confine most comments to temperature from this point.

The modeled profiles show the same pattern of overall positive meridional gradients and steplike variation in the bottom level as do the Levitus data; however, there are differences between the traces for different channel treatments. The channel types are referred to as blocked, diffusive, semiadvective, and advective. As the topography was changed from blocked to successively more open members of this series, the size of the steps decreased monotonically. The strength of bottom currents within the basins also changed monotonically through the series ([Fig. 4](#)). It is convenient to consider the end members of the series first and the intermediate types afterward.

#### 1) BLOCKED CHANNELS

With ridges blocked below 3700 m, bottom water cannot flow from basin to basin at the bottom level; however, this does not mean that the water at the deepest level need be stagnant. In each of the basins, there was a northward bottom current, intensified toward the western boundary, with vigorous downwelling associated with convection and destratification at the southern end and with upwelling in the boundary current and toward the northern end ([Fig. 4a](#)). The flow followed the general direction that the AABW would be expected to take; however, because there was no preferential access of dense water via the channels of the western trough, unrealistic bottom flow to the north was found in the Angola Basin and to the northwest in the southern part of the NE Atlantic Basin.

At the South Scotia Trench, an almost unstratified AABW layer extending over levels 11 and 12 was able to flow without dilution over the ridge into the Argentine Basin. North of 50°S, only a part of the bottom level flow continued across each ridge. At these latitudes, the AABW was mostly confined to the bottom model level, the predominant water movement at level 11 being that of the southward-flowing lower NADW along the western margin ([Fig. 5a](#)). Because of the influence of the deep boundary current, water upwelling at the locations of the (blocked) Vema Channel and Ceara rise (which happen to lie close to the western boundary) did not flow northward across the ridges but recirculated within the Argentine and Brazil Basins, respectively. However, there was a current carrying 2–3 Sv of nonrecirculated water across the eastern part of the Rio Grande Rise. This current, which at level 11 was localized or intensified in the vicinity of the ridge and fed a bottom current in the Brazil Basin, may be considered an exposure of a continuous northward bottom water flow.

Since bottom water overflowing the Rio Grande Rise was at a lower temperature than that of the return flow (mostly at level 10), the Antarctic cell was able to effect a net meridional advective heat transport across the ridge. In addition, there was considerable diffusive transport associated with the sharp temperature gradient across the ridge. Antarctic properties were transmitted northward by the upwelling of cold water south of the ridge (upward cold advection), horizontal transport across the ridge (northward cold advection and diffusion), and convection into the bottom level in the downwelling water north of the ridge (downward cold diffusion). Diffusive transmission can occur even when there is no overflowing current. The transmission of Antarctic properties across ridges is inefficient because the overflow pathway, where it exists, is not well insulated against lateral diffusion and advection from the recirculating deep water north of the ridge, and diffusive fluxes can only occur where there is a temperature difference. The poor communication is seen in the stepped profile of the bottom level temperatures, whose values rise to meet those of the level above at the top of each step, that is, immediately to the north of the ridge ([Fig. 3a](#)). Diffusion and overflows transmitted an Antarctic influence in the western trough at least as far as the Ceara rise. Beyond this point, insufficient density contrast remained to drive an overturning cell in the Northwest Atlantic Basin, which as a result was filled with NADW, making it warmer and more saline than observed.

In spite of a northward increase in temperatures and salinities from one basin to the next, there was an anomalous reversal of tracer gradient within each of several of the basins. The low temperatures at the northern ends of the basins were a

spurious effect caused by the inability of prescribed vertical diffusivities to stabilize the centered advection scheme in regions of strong upwelling. This problem is analyzed in Part II.

## 2) ADVECTIVE CHANNELS

Channels in the model topography that are continuously two cells wide (Fig. 2a) permit currents, and hence advective fluxes, to pass between one basin and another; in this study they are referred to as “advective” or “open.” When the major fracture zone channels were represented by advective channels at the bottom model level, a continuous flow of AABW was created via these connections from the Weddell Sea into the NW Atlantic Basin, and from the western trough into the Angola Basin and the NE Atlantic Basin (Fig. 4d). None of the northward bottom water transport crossed over the blocked parts of the ridges. Modeled transports for some of the channels are compared with observed values, where available, in Table 1 (1 and 2); also included are results for some other experiments, discussed later. Figures in the observational studies have mostly been based on a temperature limit of about 1.9° or 2°C. For the model, the vertical resolution did not permit this, and it was more convenient to take the AABW as being confined to the 12th model level (the top of which is at 3700 m and fairly close to the observed 2°C isotherm north of 30°S). The bottom-water mass transport at each constriction was calculated by summing the tracer advective mass transports across a line of cell faces spanning the channel at the 12th model level. Transports were generally of the right order of magnitude.

The jump in tracer values at the Vema Sill was much reduced, and those at the Ceara rise, Romanche Fracture Zone, and Vema Fracture Zone were absent (Fig. 6), causing bottom tracer values in the Brazil, Angola, and NW Atlantic Basins to be lower than in the blocked channel case by 1°–2°C and 0.1–0.2 psu and unacceptably low compared to observations. North of 30°S, the overlying layers were also cooler and fresher, but in diminishing intensity with height to a depth of 2000 m from the surface. A similar response occurred in the western part of the Indian Ocean, where parallel changes in bottom topography were made. Changes in other parts of the ocean were obscured by the restorative effects of the interior forcing; however, in tests performed without it, the Antarctic Circumpolar Current (ACC) was found to be warmer over most of its depth by a few tenths of a degree owing to drainage of AABW into the Atlantic basins and away from the Southern Ocean.

With open channels, a bottom current flowed northward along the south eastern arm of the NW Atlantic Basin and along its eastern margin to 30°N. On this model grid, the whole south eastern arm is effectively a 2-cell wide channel, and the bottom water properties were subject to progressive change due to frictionally induced downwelling on the southern side and upwelling along the midocean ridge. This gave the meridional profile a steady gradient, which is not seen in the Levitus data.

The large temperature depressions in the northwestern corners of the Argentine and Brazil Basins have been reduced to small isolated occurrences; however, those along the western side of the Cape Basin, from which no exits were introduced, and along the western side of the Brazil Basin are still present. In a run with interior forcing removed, the bottom current continued to the northern end of the NW Atlantic Basin, where it upwelled, causing a large temperature depression.

## 3) SEMIADVECTIVE CHANNELS

An opening needs to be continuously at least two cells wide to allow continuity of velocity vector points (and hence alongstream advection and diffusion of momentum, if these are considered important). However, tracer fluxes are possible through channels of a single grid cell width. There are two types of single width channel, and they have different properties. In the case of Fig. 2b, the topographic points lie diagonally on either side of a central grid cell. Because advective fluxes are calculated from velocities averaged to the centers of grid faces, each of which is capable of receiving a finite contribution from one of the two diagonally situated velocity points, a net horizontal tracer transport is possible through the square. For instance, in a diagonal opening aligned NW–SE, it is possible for the current vectors at the ocean velocity points on both the NW and SE corners of the central grid cell to be directed northwestward, creating the advective fluxes on the four faces necessary for a continuity of heat transport. Such an alignment of velocities can be seen to have arisen at the South Sandwich Trench and Ceara rise in Fig. 4c. With suitably balanced velocities, there need be no horizontal convergence in the central square, and hence no vertical motion and advection. The arrangement just described is referred to as a “semiadvective channel” (for want of a better term). It will be seen to have a good fraction of the efficiency of a full advective channel in depressing temperatures in the northern basins (Fig. 3).

There are two factors that can be expected to limit this efficiency. The first is that there will be greater friction because of the greater interaction with topographic points near the gap, and hence reduced mass transports (See Table 1). The second is that, while tracers may be advected through the gap, the cross-channel tracer gradients, may not. This tends to make the flow turn anticyclonically on passing through the opening, that is, to the left (right) in the Southern (Northern) Hemisphere, inducing a horizontal or vertical inflow of warm water on the cyclonic side, which reestablishes the cross-stream pressure gradient. That the inflow was, in fact, only vertical and in the expected sense (downwelling on the right in the SH at the South Sandwich Trench, the Vema Sill and the Atlantic–Indian Ridge, and on the left in the NH at the Ceara rise) can be clearly seen in Fig. 4c. Upwelling on the anticyclonic side of an opening occurred in association with this, but this tended to be on the upstream side of the ridge or, if on the downstream side, to be less intense. Vertical advection associated with these motions resulted in warmer bottom temperatures north of the ridge, as can be seen to be the case in the traces in Fig. 3. Similar but weaker pairs of upward and downward velocities can also be seen in the advective channel velocities (Fig. 4d).

## 4) DIFFUSIVE CHANNELS

The single-width channel geometry shown in [Fig. 2c](#) is able to transmit diffusive fluxes, but not advective fluxes, since velocities on either side of the cell face forming the aperture, and hence advective velocities through the aperture, are zero. The jumps in temperature across the ridges were greater than in the advective and semiadvective channel cases; however, because of diffusion through the gaps, they were less than in the blocked ridge case, and there was no longer a coincidence of properties at the two levels on the downwelling side of each gap ([Fig. 3](#)). The vertical stratification that was thus maintained in the water north of the Ceara rise induced a convective circulation, which brought some Antarctic influence into the NW Atlantic Basin; however, the northward flowing bottom current was weaker and more rapidly diluted by vertical advection than in the advective channel case.

The intensification of property gradients at the openings is necessary to allow diffusion through the gaps to balance the advective transport carried by the vertical circulation within each basin. Some values of temperature, mass transport, diffusive transport, and grid cell tendency are given for the Ceara rise in [Fig. 7](#). Cold advection–warm diffusion occurred at both levels in the upwelling water on the south side (left), and warm advection–cold diffusion on the north side. Note that vertical diffusion played a very minor role in this process and that convective adjustment had been shut off and was not contributing to it on the downwelling side. The buoyancy forcing needed to drive a vertical convective cell in the ocean is normally brought about by diffusion into the column from above or below, but in this case the diffusion was almost entirely horizontal. The mechanism is that of a naturally forced heat exchanger in which downwelling warm water at the upper level on one side of the ridge loses buoyancy to the cold water moving in the opposite direction on the other side, causing the former to sink and the latter to rise. The pairing of upwelling on the cold side and downwelling on the warm side is clearly visible for most of the openings in [Fig. 4b](#). The efficacy of the exchange mechanism is not dependent on a direct (essentially northward) current across the opening at the upper level; at the Ceara rise, the current is, in fact, southward. The convective cells in adjacent basins may be independent, and the arrangement would work even if the diffusive opening extended to the surface. When there is a direct cross-ridge current, whether straight above the opening or away from it, there may also be a northward advective transport associated with a warmer return flow at other levels. At the Vema Sill, the creation of a diffusive gap increased the currents within the basins and induced a small anomalous northward flow above the gap, but the flow across the eastern part of the Rio Grande Ridge decreased ([Fig. 5b](#)).

## 5) AUTOMATED TOPOGRAPHY

When topography is generated automatically, channels will not all be resolved in the same way. In a separate experiment, topography was generated at model resolution as described in [section 2](#), and the openings in the Atlantic Ocean at level 12 were as given by the interpolating program. This produced fairly wide openings at the South Sandwich Trench and Atlantic Indian Ridge but mostly blocked ridges elsewhere. Because the South Sandwich Trench has very little influence on bottom-water properties while the constrictions farther north do, the temperature profiles were almost the same as in the blocked ridge case, except for much lowered temperatures in the Cape Basin.

### *b. Twenty-one-level experiments*

Experiments were also conducted with a 21-level model. Normally one would generate a higher resolution independently from topographic data, but, to keep the solutions comparable, the same topography, and hence the ocean volume and deep basin connections, was used as in the 12-level experiments. This was done by assigning the masks used in the 12-level model to pairs of levels in the 21-level model (i.e., the level 4, 5, . . . , and 12 masks of the former to 4 and 5, 6 and 7, . . . , and 20 and 21 of the latter). Simulations were performed with the bottom channels blocked or resolved as in the 12-level experiments, the topography at levels 20 and 21 being the same in each case. In addition, one simulation was performed with an advective channel open at level 20 only, level 21 being blocked by a sill at 4150 m.

With blocked channels, the profiles for levels 20 and 21 were similar in form to that of the corresponding single level for the 12-level model, but the spurious temperature depressions were, as expected, much less, making the average basin temperatures higher ([Fig. 8](#)). The slightly lowered temperatures north of the Ceara rise were caused by a northward cross-ridge flow of 1 Sv, resolved on the subdivided grid. The availability of an extra level in the depth range 2800–3700 m allowed bottom-water overflows to occur (at level 19) across the blocked Vema Sill, the Walvis Ridge, and the Mid-Atlantic Ridge near the equator. The near coincidence of the curves for levels 20 and 21 was due to convective adjustment: at the southern ends of the basins, this was caused by dense overflows; at the northern ends, by spurious temperature depressions at level 20 upwelling points.

In the open channel case, the northward flow at most latitudes was bottom intensified as a result of the coldest water at the levels 20 and 21 being on the anticyclonic side. North of the equator, the lower level carried nearly all of the northward current, which extended to the northern ends of the troughs. Differential advection explains why temperatures in the bottom 450-m layer were 0.4–0.7°C colder than in the layer above north of 30°S. The channel transports ([Table 1](#), col. 6) were comparable with the 12-level figures. The temperature curves were similar in form to the one seen with the 12-level model, except in the NW Atlantic Basin, where increased bottom-water penetration caused temperatures to be lower.

With the lowest level blocked by a sill at each channel, the increases in temperature at the ridges at both levels were more pronounced than with open channels. One might infer from the profiles that level 20 water was overflowing each sill into level 21 on the other side; but actually most of the northward mass transport north of the Vema Sill was in level 21, and the only appreciable flows at level 20 were where water from the lowest layer rose to cross the sills. At these latitudes, the channel transports at level 20 across the sills were not much smaller than the total transports for levels 20 and 21 with open channels. The warming of the water as it passed over each sill was due to advection and horizontal diffusion. The sharpened horizontal gradients at level 20 indicate that diffusion came from the north of the sill region. Although horizontally oriented,

this diffusion is considered to be important in sill overflows. The process is the same as that encountered with water overflowing at 3700 m in the blocked channel experiment. However, in the present experiment, the overflows were locked to the locations where the channels were provided (at level 20), and the mixing occurred at a level that was within the AABW.

The results of the 21-level integrations can be used to quantify the relative efficiencies of the transmission of Antarctic properties by advective and diffusive channels since these are much less confounded by the effects of numerical temperature depressions. For a fair comparison, the two types of opening needed to be of the same width, so an experiment was also performed in which the diffusive channels were made two cells wide. To arrest the flow while still allowing tracer diffusion to operate, the bottom velocity point at the center of the channel was made a topographic point, while the surrounding tracer points were maintained as ocean points. The 3700–4600 m depth-averaged profiles for the various channel treatments (Fig. 9) show the same monotonic progression as with the 12-level model, but more clearly, because of the relative absence of temperature depressions. Basin currents showed a similar sensitivity. Total northward bottom transport at 15°S (about half way along the Brazil Basin) with different types of channel were: blocked, 3.0; diffusive single width, 3.6; diffusive double width, 3.9; semiadvective, 4.5; and advective, 5.1 Sv. Although the relative response differed between basins, one could say that, relative to the blocked case, double-width diffusive channels produced temperature changes about half of those produced by advective channels. This should not be taken to imply that diffusive and advective transports with advective channels are comparable. The calculation of net meridional transports due to the spreading of AABW strictly requires a knowledge of its return flow, which is not closed or well defined; however, an estimate based on average gradients indicates that the diffusive transport ( $3 \times 10^{12}$  W) is an order of magnitude smaller than the advective transport ( $30 \times 10^{12}$  W). The balance is similar in the diffusive channel case, but only within the basin interiors, not at the choke points. The efficacy of diffusive channels consists in the fact that temperature gradients at the ridges are large but spatially confined, creating sufficient diffusion locally to drive invigorated convective circulations and advective heat transports in the basins (See Fig. 7).

#### 4. The effects of channel dissipative coefficients

While the advective channel model reproduced observed channel transports reasonably well, it was not able to simulate the observed changes in tracer values between basins. This may be because tracer gradients in channels are determined by a number of processes that depend upon the speed and narrowness of the stream. In a global model, it is not possible to make the channels as narrow or the current velocities as strong as they are in reality. In fact, considering that the eddy viscosity is usually made just large enough to resolve western boundary currents over a width of one or two grid squares, it may well be that current speeds, and hence the controls exercised by the channel, will not be much greater than within the basins. To compensate for this bias, some modification of channel properties may be justified. It has already been seen that temperature gradients may be controlled in a coarse way by making changes to the channel geometry. Control is also possible in advective channel simulations by parameterizing the mixing effects of the unresolved topography. In this section this is done in a fairly simple way by adjusting diffusive or viscous parameters locally at the channel grid points.

##### *a. Effects of changing vertical diffusivity at openings*

It is not axiomatic that most of the tracer variation should occur in the connecting channels rather than in the basins. Considering only the downward diffusion of heat, the fact that the movement of water in the basins is slower than in the channels would tend to keep most of the temperature variation within the basins. On the other hand, observations show the largest horizontal tracer gradients to be across the midocean ridges and at the deepest levels. Between the western and eastern ends of the Romanche Fracture Zone, the temperature at 4500 m changes by about 1°C, while at 4000 m the change is only 0.2°C. One obvious explanation for large tracer gradients that has already been considered is the effect of sill depth in preventing the densest upstream water from passing into the next basin. Another is that turbulence caused by the rapid flow of water as it passes across the sill and cascades into the next basin will generate strong vertical mixing and warm the bottom water as it passes through the gap. Polzin et al. (1996) have obtained evidence of this mixing from dissipation data and have calculated a diffusivity of  $150 \text{ cm}^2 \text{ s}^{-1}$  in the water below 4000 m downstream of the main sill. Mixing in a channel will tend to amplify the horizontal temperature difference between the bottom waters due to the blocking action of the sill. Speer et al. (1994) have commented that sill depths have been underestimated in the past by an interpretation of such temperature differences as evidence that the flow is blocked at a particular level.

To investigate the response to enhanced vertical mixing, the vertical diffusivity between levels 11 and 12 above just the two grid cells spanning each gap was increased from its normal value of  $1 \text{ cm}^2 \text{ s}^{-1}$  to 10, 100, and  $10^6 \text{ cm}^2 \text{ s}^{-1}$  (the last value representing complete mixing of the selected grid columns). The enhanced mixing produced sharpened gradients, and in some cases locally maximum temperatures, at each gap, and a consequent general rise in bottom temperatures north of 30°S, reaching 0.2°, 0.7°, and 1.2°C in the Tropics and in the eastern trough with diffusivities of  $K_H = 10, 100, \text{ and } 10^6 \text{ cm}^2 \text{ s}^{-1}$ , respectively. However, temperature anomalies near the openings at the level above were of opposite sign to those at the bottom level: this response differs from that which occurred with changes of channel topography, where cold anomalies at the bottom level were associated with weaker and more general cold anomalies at the level above.

In the meridional profiles, a temperature jump is seen at the Vema Sill but not at the northern end of the Brazil Basin, where sharp meridional gradients were confined to the western margin (Fig. 10). A large vertical diffusivity was required to produce much effect. Although of the same order as the value Polzin et al. calculated, a diffusivity of  $100 \text{ cm}^2 \text{ s}^{-1}$  would

be very large when applied to the mixing between two grid cells 300 km wide and 900 m deep, but, even with this value, the horizontal temperature difference across the Romanche Fracture Zone was only about  $0.15^\circ$ . (The 21-level sill simulation represented this channel better, with a  $0.6^\circ\text{C}$  temperature change at 4375 m and  $0.15^\circ\text{C}$  at 3925 m.) A possible explanation for the poor depiction of temperature gradients is that strong meridional circulations (upward in the mixed columns and downward to the south) were set up by the localized density changes generated by the mixing, notably at the Ceara rise and the Romanche Fracture Zone. These circulations would have caused an exaggerated increase in channel flows and strong downward resolved scale stirring in the basin to the south of each opening, which would have tended to spread the temperature change over a wider area.

### *b. Effects of changing horizontal diffusivity at openings*

In a narrow channel, turbulence would tend to make the diffusivity larger than in the basins, not only in the vertical, but in the horizontal. On its own, this would tend to reduce temperature gradients in the channel relative to those in the basins; however, in a constriction between two basins, the current is also increased, and this also has an effect on tracer gradients. In an isolated stream in advective–diffusive equilibrium, the temperature diverges exponentially from an upstream asymptotic value with an amplification rate (inverse  $e$ -folding length)  $u/A_H$ . It is shown in Part II that, when this quantity changes, the temperature gradient changes by the same factor. Because the current increases by a much greater factor than the diffusivity, the temperature variation would actually be *sharpened* in the channels. For instance, a 5 Sv transport of a 1000 m deep current through a channel 50 km wide would have a speed of  $10\text{ cm s}^{-1}$  and an amplification length of  $A_H/u = 10\text{ km}$ . Since this is rather less than the typical length of a fracture zone channel, most of the temperature change would occur just before the water reached the exit, or immediately after emerging into the downstream basin. Within the basins themselves, water is homogenized by gyre circulations or by the effect of mesoscale eddies, which in coarse resolution models is parameterized as diffusion. In a basin 1000 km wide the diffusive scale length would be 200 km but, if the effect of gyre stirring were included, it might be closer to the size of the basin. Thus the gradients near the channel exits could be 20–100 times greater than in the basins.

Because of the excessive width of resolved channels, modeled values of  $u$  are too small to obtain a suitable diffusive length. To counteract this,  $A_H$  would need to be made smaller, not larger (but only in the direction of the current—the scaling of cross-channel diffusivity required for a realistic erosion of geostrophic gradients is the opposite of this).

Unfortunately, modeled channel currents (of order  $1\text{ cm s}^{-1}$ ) are close to the horizontal Péclet limit anyway; a diffusivity calculated to give the length scale of 10 km computed above would give a horizontal grid Péclet number of 30. It is shown in Part II that increases in  $u/A_H$  do not translate into increased gradients in the finite difference solution at large grid Péclet numbers. This was confirmed in an experiment in which the diffusion at the pair of interfaces across each opening was set to zero. The response was a small lowering of temperature of up to  $0.1^\circ\text{C}$  on the upstream side of each gap (which created or intensified a local minimum there) and some compensating adjustments in neighboring cells, but very little change elsewhere.

### *c. Effects of changing friction at openings*

With coarse grid spacing, it is not possible to simulate the hydraulic control of a flow in which accelerative terms are important. Fortunately, this may not be necessary. [Whitehead et al. \(1974\)](#) have shown that in a rectangular channel wider than the internal Rossby radius (about 20 km), as it is in most cases, the maximum volume flux is that which can be transported by a horizontally stratified geostrophic current,

$$Q = \frac{g'H^2}{2f},$$

where  $g' = g\Delta\rho/\rho$  is the reduced gravity based on the density variation across the channel and  $H$  is the depth of the channel beneath an assumed level of no motion. Ocean models reproduce the dynamics embodied in the above formula, as [Wadley and Bigg \(1996\)](#) have demonstrated for the case of a channel of one velocity point width, having made allowance for a halving of the transport because of the no-slip boundary condition in the Bryan–Cox model. A fortunate feature of the formula is that the transport is independent of the channel width, and the main question will then be how well models can reproduce the cross-channel density gradient that drives the current. However, this independence will not obtain if frictional effects are important.

Applying the above formula to estimates of channel dimensions and density range, [Whitehead \(1989\)](#) calculated transports of 16.3 Sv across the Vema Sill and 4.6 Sv across the Ceara rise. These are rather higher than observed values (cf. [Table 1](#)); however, the degree of frictional control that he thought that this discrepancy might imply is uncertain, because [Killworth \(1992\)](#) showed that the maximum exchange is dependent on channel geometry and that more realistic transports were obtained for these sills using a parabolic or V-shaped channel profile.

Lateral friction in the model varies with channel width,  $\Delta x$ , as  $1/\Delta x^2$  (or as  $1/\Delta x$  when the inverse variation of velocity with  $\Delta x$  is taken into account), but this reduction with width is to some extent offset by the large eddy viscosities used with coarse resolution for numerical reasons. At most latitudes, the horizontal friction term is only a small fraction [ $2A_H/(f\Delta x^2) \approx 0.1$ ] of the Coriolis term, and the vertical friction term (including bottom drag, if applied) is even less. Although its direct



effect on modeled transports is small, channel friction also has another effect, and that is to realign the isotherms in such a way as to produce a component of the temperature gradient along it. The warming of the water is brought about by vertical advection caused by downwelling on the cyclonic side after the gap, as can be seen in [Figs. 4d](#) and [6](#). The realignment will either reduce the geostrophic pressure gradient (and hence the transport) or cause the total tracer changes along the channel to increase (or, most likely do both) when the density differences along the channel become comparable with those across the channel. In a channel rather longer than wide, as a number of the interbasin channels actually are, this will happen with a small relative frictional force. In channels that can reasonably be designed into a coarse-resolution ocean model, the dimensions are about equal, and, for the isotherms to be substantially cross-channel, friction forces need to be dominant, that is, increased by a factor of 10 or more (less near the equator). Since only the bottom level was involved, this was most conveniently done by setting a large linear bottom drag coefficient at the channel points. For a 900 m bottom layer in midlatitudes, friction and Coriolis terms become comparable when  $C_D = f\Delta z \approx 10 \text{ cm s}^{-1}$ . Channel flows for this level of drag are shown in [Table 1](#) (col. 4) to be reduced in most cases by a factor of about  $\frac{2}{3}$ , which is close to the value of  $(2)^{1/2}$  expected assuming no change in pressure gradient force. Drag coefficients used in the experiments were  $C_D = 10, 30,$  and  $60 \text{ cm s}^{-1}$ . The case of an effectively infinite drag is represented by the 2-cell-wide diffusive channel (zero flow) simulation, described earlier.

The enhancement of channel friction did not improve modeled transports, which were close enough to observed values in the control simulation, but it did have a beneficial effect upon the temperature distribution. The bottom temperatures for the western Atlantic obtained with different drag coefficients are shown in [Fig. 11](#); also included is the curve for the semiadvective channel case. Increased drag caused the temperature jumps at the interbasin ridges to become larger and more like those seen in the Levitus profile. The semiadvective channel configuration produced a similar response, the effect on temperatures and currents (see [Table 1](#)) being equivalent to an advective channel with a bottom drag of about  $15 \text{ cm s}^{-1}$ . Relative to the standard open channel case, both methods of increasing channel resistance produced progressively warmer conditions in the northern basins and less penetration of the AABW current into the NW Atlantic Basin. In this basin, neither method achieved the relatively isothermal conditions seen in the Levitus data.

## 5. Conclusions

Fracture zone channels give AABW access to deep basins of the Atlantic Ocean and are important in determining the temperature distribution of the latter. These channels may or may not be resolved in the model topography. Differences between blocked and open channel simulations show that modeled bottom tracer values are quite sensitive to the representation of topographic barriers and that responses of smaller magnitude may be felt in the NADW and ACC.

The blocked ridge topography prevents any flow below 3700 m between basins, that is, at the depths in which AABW is found, but this does not prevent the spreading of water with Antarctic properties from basin to basin. A proportion of the water flowing northward in each basin upwells and overflows the ridges, and to that extent the basin currents may be considered to be part of a distorted but continuous bottom current; the remaining water upwells and flows back within each basin in a basin-scale vertical convective cell. The net flow northward across the ridges at 30°S is 2–3 Sv, which is a good proportion of the flow through the Vema Sill in the open-channel experiment. However, the transmission of Antarctic properties is inefficient. Relative to the bottom-water stream, there is considerable mixing at the overflows with water recirculating within the basins, both by advection and horizontal diffusion. These processes maintain a temperature gradient across each ridge; hence, much of the heat exchange between basins is diffusive. The result is a profile of meridional bottom-level tracer variation that is sharply stepped at the interbasin ridges in the Atlantic. The process is inefficient to the extent that it is not able to carry the Antarctic influence into the northwest Atlantic, which is consequently too warm and saline at depth. Because automated topography generation for coarse-resolution ocean models tends to produce a topography in which channels connecting basins below 4000 m are not resolved, it is likely that many models may suffer from this defect.

The inclusion of interbasin channels in models gives them a chance to simulate the spreading of this water mass in a natural way, along the correct paths between basins, and with limited interaction between AABW and the deep water above. Unfortunately, the bottom simulation with open channels is also poor, except that in this case it is because temperatures are just about everywhere too low. With blocked ridges there is too much interaction with the overlying waters; with open channels, too little. The chief deficiency of the open-channel simulation is the failure of the model to represent the sharpness of the interbasin temperature gradients. These very much depend on mixing processes in rapid currents. Modeled interbasin transports in the open-channel simulation are of the right order, which is important because, for basins of given size, these transports will correspond to particular residence times and upwelling rates. However, with channels so much wider than they are in nature, a realistic mass transport automatically means that current speeds will be far too small and that controls of the flow and the mixing will not be properly represented.

To overcome this problem, it was decided to parameterize channel processes by making local modifications to the geometry or exchange coefficients at the openings. Although physically reasonable, local changes to diffusivities did not provide the right response. The enhancement of vertical diffusivities at interbasin channels was able to produce sharpened gradients in bottom-water properties; however, large diffusivities were required to give an adequate response and the temperature changes were not very tightly localized at the interbasin channels. This, coupled with the inverse temperature variation at the upper level and the unusual vertical circulation induced, makes this a less than satisfactory parameterization of channel effects. Horizontal diffusivity is another parameter that can be altered, but it has been shown that an adjustment to compensate for the underrepresentation of channel velocities requires the eddy diffusivity to be reduced, creating a violation of the horizontal grid Péclet condition.

Increasing the channel friction provides another means of manipulating tracer distributions. Frictional forces not only retard the flow, but tend to realign the isotherms, which increases the interbasin temperature gradients. A helical movement is induced in the channel and in the level above it, which warms the bottom level on the cyclonic side from above by vertical advection, thus helping to maintain the cross-stream pressure gradient. With normal viscosity, the flow is fairly geostrophic, and so, with channels that are of necessity only one grid cell in length, the effect is not very great. Choosing a level of bottom drag in the range of frictional dominance produced a more realistic progression of temperature changes at ridges, but at the expense of degrading what were otherwise realistic channel flows.

It has been shown that single-width channels are capable of transmitting either diffusion only (diffusive channels) or diffusive and limited advective fluxes (semiadvective channels) depending on their geometry. This arises because the arrangement of variables on the Arakawa B grid. The resistance to flow induces vertical motions and a compensation of advective by diffusive fluxes, and hence increased tracer gradients. The effects are similar to those produced by changes in channel friction. When basins are linked by single-width channels, meridional profiles intermediate between those of the blocked and open-channel topographies are produced. Because these openings occur randomly and at different levels in topography generation, it would be wise for modelers to understand their properties and to eliminate or widen them manually if they are considered to distort the circulation. Alternatively, these channels may be included by design where space is limited or where a coarse degree of control over tracer gradients is desired. Single width openings could also be used for surface channels, in order to resolve the Strait of Gibraltar, for instance. In some models, such surface channels may be forbidden at model initialization because of difficulties in mapping coastlines for island streamfunction relaxation. If such difficulties can be overcome, there is no reason that surface diffusive channels should not be included. Semiadvective channels should only be used for passages to embayments since barotropic mass fluxes would not be admitted.

In the 21-level integrations, the responses of channel transports and bottom temperature profiles to changes in channel geometry were similar to those found in the 12-level integrations; however, the ocean solutions were superior in certain respects. The most obvious was in the mitigation of numerical problems, which in the deep ocean were found to be particularly associated with flows over topography. In the abyssal basins, increased vertical resolution allows some bottom intensification of currents and differential advection, which may help to spread the AABW and keep the water at different levels in each basin more independent and uniform. A particular deficiency in all the 12-level solutions (except the blocked case, where there was no AABW penetration) was the continuous meridional temperature gradient in the NW Atlantic Basin; this was due to the interaction of water masses entering opposite ends of the basin and is a feature not found in the Levitus profiles. Extra resolution was successful in leveling the temperatures to some extent, but part of the problem may be lack of horizontal resolution, which makes boundary currents too wide and friction too great in the narrower parts of the basin.

Where sufficient vertical resolution is available, as it is in the 21-level model, control of transports and gradients is possible by narrowing the channels vertically, that is, by inserting sills that are shallower than the basins but deeper than the ridges they intersect. The 21-level grid provides a layer interface at 4150 m, which is a suitable level for a blockage and well within the depth range of AABW. An experiment with this configuration was successful in creating realistic temperature contrasts between the basins, but the way that this was achieved was not by blocking the denser water classes below the sill. Rather, the overflowing water originated from the upwelling of water from the bottom level, which was warmed by advection and horizontal diffusion (essentially a form of enhanced diapycnal mixing) as it moved in the upper level across the sill. This also happened with ridges blocked to 3700 m; however, having sills below the level of the ridge resulted in less mixing with deep water and greater control over the route taken by the spreading of bottom water. For this control to be effective, the positions and depths of both sills and ridges need to be adjusted following topographic interpolation.

A number of means of controlling tracer gradients has been considered. Essentially, all of the measures have the effect of controlling the extent to which AABW and NADW are stirred in the region of the openings—whether by direct downward diffusion, by horizontal diffusion of heat vertically diffused or advected in the basin interiors, or by local vertical advective circulations induced by frictional effects. These measures tend to generate vertical motions that are possibly unrealistic, but one could argue that the latter can be tolerated provided that they allow the appropriate degree of mixing and a better solution. The experiments have indicated the sensitivities of these interventions, but these would change if the model resolution, forcing, mixing parameters, or mixing scheme were different. The modeler needs to look carefully at the effects of introducing various topographic modifications or local mixing enhancements and select the means that are most appropriate.

#### *Acknowledgments*

Funding from the Antarctic Science Advisory Committee administered by the Australian Antarctic Division of the Department of the Environment, Sport, and Territories is gratefully acknowledged.

---

#### REFERENCES

- Bryan, K., 1969: A numerical method for the study of the circulation of the world ocean. *J. Comput. Phys.*, **4**, 347–376.
- , 1984: Accelerating the convergence to equilibrium of ocean–climate models. *J. Phys. Oceanogr.*, **14**, 666–673. [Find this article online](#)
- , S. Manabe, and R. C. Pacanowski, 1975: A global ocean–atmosphere climate model. Part II: The oceanic circulation. *J. Phys.*

- Hellerman, S., and M. Rosenstein, 1983: Normal monthly wind stress over the world ocean with error estimates. *J. Phys. Oceanogr.*, **13**, 1093–1104.. [Find this article online](#)
- Hirst, A. C., and W. Cai, 1994: Sensitivity of a World Ocean GCM to changes in subsurface mixing parameterization. *J. Phys. Oceanogr.*, **24**, 1256–1279.. [Find this article online](#)
- Hogg, N., P. Biscaye, W. Gardner, and W. J. Schmitz, Jr., 1982: On the transport and modification of Antarctic Bottom Water in the Vema Channel. *J. Mar. Res.*, **40**, 231–263..
- Killworth, P. D., 1987: Topographic instabilities in level model OGCMs. *Ocean Modelling* (Unpublished manuscripts), **75**, 9–12..
- , 1992: Flow properties in rotating, stratified hydraulics. *J. Phys. Oceanogr.* **22**, 997–1017..
- Levitus, S., 1982: *Climatological Atlas of the World Ocean*. NOAA Prof. Paper No. 13., U.S. Govt. Printing Office, 173 pp..
- McCartney, M. S., S. L. Bennett, and M. E. Woodgate-Jones, 1991: Eastward flow through the Mid-Atlantic Ridge at 11°N and its influence on the abyss of the eastern basin. *J. Phys. Oceanogr.*, **21**, 1089–1121.. [Find this article online](#)
- Mercier, H., and K. G. Speer, 1998: Transport of bottom water in the Romanche Fracture Zone and the Chain Fracture Zone. *J. Phys. Oceanogr.*, **28**, 779–790.. [Find this article online](#)
- Moore, A. M., and C. J. C. Reason, 1993: The response of a global ocean general circulation model to climatological surface boundary conditions for temperature and salinity. *J. Phys. Oceanogr.*, **23**, 300–328.. [Find this article online](#)
- Murray, R. J., and C. J. C. Reason, 1999: Influences of topography on the modeling of abyssal water masses. Part II: Spurious Extrema. *J. Phys. Oceanogr.*, **29**, 2872–2885.. [Find this article online](#)
- NCAR Oceanography Section, 1996: The NCAR CSM Ocean Model. NCAR Tech. Note NCAR/TN-423+STR, 75 pp..
- Polzin, K. L., K. G. Speer, J. M. Toole, and R. W. Schmitt, 1996: Intense mixing of Antarctic Bottom Water in the equatorial Atlantic Ocean. *Nature*, **380**, 54–57..
- Saunders, P. M., 1987: Flow through Discovery Gap. *J. Phys. Oceanogr.*, **17**, 631–643.. [Find this article online](#)
- Speer, K. G., and W. Zenk, 1993: The flow of Antarctic Bottom Water into the Brazil Basin. *J. Phys. Oceanogr.*, **23**, 2667–2682.. [Find this article online](#)
- , H. Mercier, M.-J. Messias, and L. Mémer, 1994: The Romanche Fracture Zone: Blocking and mixing of Arctic and Antarctic waters at the equator. *Int. WOCE Newslett.*, **16**, 8–11..
- Thompson, S. R., 1995: Sills of the Global Ocean: A compilation. *Ocean Modelling* (Unpublished manuscripts), **109**, 7–9..
- Tomczak, M., and J. S. Godfrey, 1994: *Regional Oceanography: An Introduction*. Pergamon, 422 pp..
- Wadley, M. R., and G. R. Bigg, 1996: Abyssal channel flow in ocean general circulation models with application to the Vema Channel. *J. Phys. Oceanogr.*, **26**, 38–48.. [Find this article online](#)
- Wajsowicz, R. C., 1993: A consistent formulation of the anisotropic stress tensor for use in models of the large-scale ocean circulation. *J. Comput. Phys.*, **105**, 333–338..
- Warren, B. A., and K. G. Speer, 1991: Deep circulation in the eastern South Atlantic Ocean. *Deep-Sea Res.*, **38**, S281–322..
- Whitehead, J. A., 1989: Internal hydraulic control in rotating fluids—Applications to oceans. *Geophys. Astrophys. Fluid Dyn.*, **48**, 169–192..
- , and L. V. Worthington, 1982: The flux and mixing rates of Antarctic Bottom Water within the North Atlantic. *J. Geophys. Res.*, **87**, 7903–7924..
- , A. Leetma, and R. A. Knox, 1974: Rotating hydraulics of strait and sill flows. *Geophys. Fluid Dyn.*, **6**, 101–125..
- Williams, G. P., 1972: Friction term formulation and convective instability in a shallow atmosphere. *J. Atmos. Sci.*, **29**, 870–876.. [Find this article online](#)
- Zenk, W., K. G. Speer, and N. G. Hogg, 1993: Bathymetry at the Vema Sill. *Deep-Sea Res.*, **40**, 1925–1933..

---

## APPENDIX

### 6. Friction Term for Spatially Varying Viscosity in Spherical Coordinates

The form of the friction tensor in the case of spherical isotropy with spatially varying viscous coefficients has been derived by [Wajsowicz \(1993\)](#). Using the shallow water approximation,  $r = a$ , in terms containing the radius of the earth, setting to zero the viscous coefficient  $\nu$ , which [Williams \(1972\)](#) has argued should be negligible in a stratified ocean, and neglecting metric terms proportional to  $K_M/a$ , her Eq. (15) may be written, with some rearrangement,

$$\begin{aligned}
 (\nabla \cdot \sigma)_x &= \frac{1}{a^2 \cos^2 \phi} \frac{\partial}{\partial \lambda} \left( A_M \frac{\partial u}{\partial \lambda} \right) + \frac{1}{a^2 \cos \phi} \frac{\partial}{\partial \phi} \left( A_M \cos \phi \frac{\partial u}{\partial \phi} \right) + \left( -\frac{2 \sin \phi}{a^2 \cos^2 \phi} A_M + \frac{1}{a^2 \cos \phi} \frac{\partial A_M}{\partial \phi} \right) \frac{\partial v}{\partial \lambda} \\
 &\quad - \left( \frac{1}{a^2 \cos \phi} \frac{\partial A_M}{\partial \lambda} \right) \frac{\partial v}{\partial \phi} + \left( \frac{1 - \tan^2 \phi}{a^2} A_M + \frac{\tan \phi}{a^2} \frac{\partial A_M}{\partial \phi} \right) u + \left( -\frac{\sin \phi}{a^2 \cos^2 \phi} \frac{\partial A_M}{\partial \lambda} \right) v \\
 (\nabla \cdot \sigma)_y &= \frac{1}{a^2 \cos^2 \phi} \frac{\partial}{\partial \lambda} \left( A_M \frac{\partial v}{\partial \lambda} \right) + \frac{1}{a^2 \cos \phi} \frac{\partial}{\partial \phi} \left( A_M \cos \phi \frac{\partial v}{\partial \phi} \right) + \left( \frac{2 \sin \phi}{a^2 \cos^2 \phi} A_M - \frac{1}{a^2 \cos \phi} \frac{\partial A_M}{\partial \phi} \right) \frac{\partial u}{\partial \lambda} \\
 &\quad + \left( \frac{1}{a^2 \cos \phi} \frac{\partial A_M}{\partial \lambda} \right) \frac{\partial u}{\partial \phi} + \left( \frac{1 - \tan^2 \phi}{a^2} A_M + \frac{\tan \phi}{a^2} \frac{\partial A_M}{\partial \phi} \right) v + \left( \frac{\sin \phi}{a^2 \cos^2 \phi} \frac{\partial A_M}{\partial \lambda} \right) u.
 \end{aligned}$$

(Click the equation graphic to enlarge/reduce size)

The equations may be rendered in finite difference form, with the aid of the operators  $\bar{\alpha}^x = (\alpha_{i+1/2,j} + \alpha_{i-1/2,j})/2$ ,  $\delta_x \alpha = \alpha_{i+1/2,j} - \alpha_{i-1/2,j}$ ,  $\delta_{2x} \alpha = \alpha_{i+1,j} - \alpha_{i-1,j}$ , etc. and the grid dimensions  $\Delta \lambda$  and  $\Delta \phi$ , as

$$\begin{aligned}
 (\nabla \cdot \sigma)_x &= \frac{1}{a^2 \cos^2 \phi \Delta \lambda} \delta_x (C_1 \delta_x u) + \frac{1}{a^2 \cos \phi \Delta \phi} \delta_y (C_2 \delta_y u) \\
 &\quad + C_3 \delta_{2x} v + C_4 \delta_{2y} v + C_5 u + C_6 v, \\
 (\nabla \cdot \sigma)_y &= \frac{1}{a^2 \cos^2 \phi \Delta \lambda} \delta_x (C_1 \delta_x v) + \frac{1}{a^2 \cos \phi \Delta \phi} \delta_y (C_2 \delta_y v) \\
 &\quad - C_3 \delta_{2x} u - C_4 \delta_{2y} u + C_5 v - C_6 u,
 \end{aligned}$$

where

$$\begin{aligned}
 C_1 &= \bar{A}_M^x / \Delta \lambda, & C_2 &= \bar{A}_M^x \cos \phi / \Delta \phi, \\
 C_3 &= \left( -\frac{2 \sin \phi}{a^2 \cos^2 \phi} A_M + \frac{1}{a^2 \cos \phi} \frac{\partial \bar{A}_M^x}{\partial \phi} \right) \frac{1}{2 \Delta \lambda}, \\
 C_4 &= \left( -\frac{1}{a^2 \cos \phi} \frac{\partial \bar{A}_M^x}{\partial \lambda} \right) \frac{1}{2 \Delta \phi}, \\
 C_5 &= \left( \frac{1 - \tan^2 \phi}{a^2} A_M + \frac{\tan \phi}{a^2} \frac{\partial \bar{A}_M^x}{\partial \phi} \right), \\
 C_6 &= \left( -\frac{\sin \phi}{a^2 \cos^2 \phi} \frac{\partial \bar{A}_M^x}{\partial \lambda} \right).
 \end{aligned}$$

The above six coefficients are all functions of  $i$  and  $j$  but, being invariant in time, may be precalculated as two-dimensional arrays so that little extra computational load is generated. When  $A_M$  is a function of  $j$  only,  $C_4$  and  $C_6$  become zero and the remaining coefficients become functions of  $j$  only; this form of the metric terms is used in the ocean component of the NCAR climate model, in which viscosities are tapered toward the poles to prevent diffusive instabilities due to diminishing grid size ([NCAR Oceanography Section 1996](#)). When  $A_M$  is constant, the equations reduce to the forms given by [Bryan \(1969\)](#) and used in the GFDL ocean model.

## Tables

Table 1. Transports (Sv) in bottom channels (symbols as in Fig. 1). (1) Observed transports, where available, (2) modeled transports below 3700 m using 12-level model with advective channels, standard parameters, and centered advection (control case), and (3)–(7) modeled flows differing from the control specifications in the following respects: (3) enhanced vertical diffusivity above channels ( $K_H = 10 \text{ cm}^2 \text{ s}^{-1}$ ), (4) enhanced friction in channels ( $C_D = 10 \text{ cm s}^{-1}$ ), (5) semiadvective channels, (6) 21-level model with channels open to bottom (total transport in levels 20 and 21), and (7) 21-level model with sills blocking level 21.

	(1)	(2)	(3)	(4)	(5)	(6)	(7)
	Obs.	Control	Enh. $K_H$	Enh. Friction	S-A channels	21-level model open	21-level model sill
VS	4 <sup>a</sup>	3.6	3.7	2.2	2.1	4.5	3.1
RFZ	1.2 <sup>b</sup>	1.2	1.5	0.8	0.9	1.2	1.3
CR	1–2 <sup>c</sup>	3.0	3.3	2.2	1.5	3.2	2.9
VFZ	2.2 <sup>d</sup>	1.5	1.9	1.0	1.2	1.3	1.2
DG	0.23 <sup>e</sup>	0.4	0.5	0.3	0.2	0.3	0.3

<sup>a</sup> Hogg et al. (1982), Speer and Zenk (1993).  
<sup>b</sup> Polzin et al. (1996), Mercier and Speer (1998).  
<sup>c</sup> Whitehead and Worthington (1982), Whitehead (1989).  
<sup>d</sup> McCartney et al. (1991).  
<sup>e</sup> Saunders (1987).

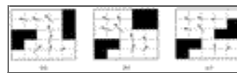
[Click on thumbnail for full-sized image.](#)

## Figures



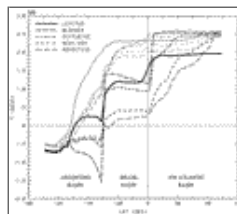
[Click on thumbnail for full-sized image.](#)

Fig. 1. Basins of the Atlantic Ocean deeper than 4000 m, showing Levitus 4000-m potential temperatures (contour interval  $0.1^\circ \text{C}$ ). Interbasin channels indicated are the South Sandwich Trench (SST), Atlantic–Indian Ridge (AIR), Vema Sill (VS), Hunter Channel (HC), Walvis Ridge (WR), Romanche Fracture Zone (RFZ), Ceara rise (CR), Kane Gap (KG), Vema Fracture Zone (VFZ), and Discovery Gap (DG). The ridge through which VS and HC pass is the Rio Grande Rise.



[Click on thumbnail for full-sized image.](#)

Fig. 2. Types of channel: (a) an advective channel, (b) a semiadvective channel, and (c) a diffusive channel. The shaded areas represent topography, the dashed lines delineate ocean tracer cells, and the arrows are possible velocity vectors at velocity grid points.



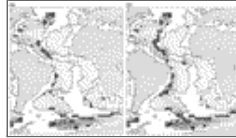
[Click on thumbnail for full-sized image.](#)

Fig. 3. Observed and modeled zonally averaged temperatures (solid and dashed curves, respectively) in (a) the western Atlantic and (b) the eastern Atlantic troughs. The heavy lines are for the 12th model level and the light lines for the 11th model level.



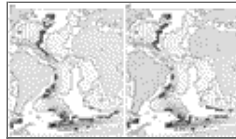
[Click on thumbnail for full-sized image.](#)

Fig. 3. (*Continued*) The traces for four model bathymetries are shown, the channel treatment in each case being indicated by the dash pattern.



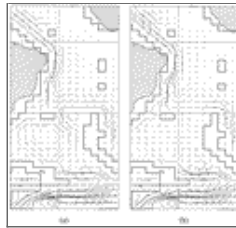
[Click on thumbnail for full-sized image.](#)

Fig. 4. Modeled bottom level horizontal velocities (1200-day streamlines) and vertical velocities (contour interval  $2.5 \times 10^{-4} \text{ cm s}^{-1}$ ) for (a) blocked channels, (b) diffusive channels,



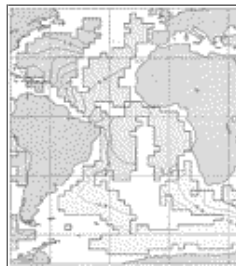
[Click on thumbnail for full-sized image.](#)

Fig. 4. (*Continued*) (c) semiadvective channels, and (d) advective channels. Vertical speeds exceeding  $2.5 \times 10^{-4} \text{ cm s}^{-1}$  are shaded, heavy for upwelling and light for downwelling.



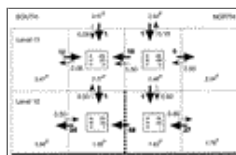
[Click on thumbnail for full-sized image.](#)

Fig. 5. Level 11 velocities, central Atlantic Ocean, for (a) blocked channel case and (b) diffusive channel case (800-day streamlines).



[Click on thumbnail for full-sized image.](#)

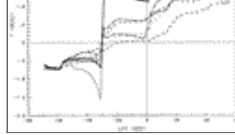
Fig. 6. Bottom temperatures for advective channel topography (contour interval  $0.2^\circ\text{C}$ ,  $1^\circ\text{C}$  band shading,  $0^\circ\text{C}$  contour emboldened).



[Click on thumbnail for full-sized image.](#)

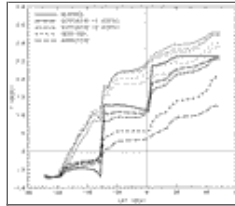
Fig. 7. Quantities associated with heat transports through a diffusive gap. The figure shows a vertical section of grid boxes across the Ceara rise at levels 11 and 12. The grid face representing the diffusive opening is indicated by a heavy dashed line. The Brazil Basin is on the left and the NW Atlantic Basin is on the right. Temperatures (in italics) are given for the grid cells adjacent to the opening (inner squares) and averages for the cells abutting them (outer squares). Interfacial mass transports (light arrows and values) are given in sverdrups. Interfacial diffusive heat transports (heavy arrows and values) and grid cell tendencies due to advection, horizontal diffusion, and vertical diffusion (in boxes) are given in units of  $10^{10} \text{ cm}^3 \text{ }^\circ\text{C s}^{-1}$  (equivalent to  $4.2 \times 10^{10} \text{ W}$ ).





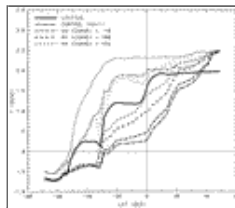
[Click on thumbnail for full-sized image.](#)

Fig. 8. Temperatures in the western trough for the bottom level of the 12-level model with channels blocked and open, and for the bottom two levels of the 21-level model with channels blocked at levels 20 and 21, open at both levels, and open at level 20 and blocked by a sill at level 21. For each of the 21-level configurations, the upper curve is for level 20 and the lower curve for level 21 (as indicated by the labels L20 and L21 where possible).



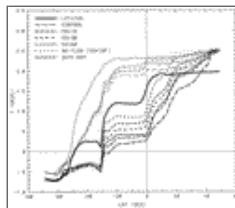
[Click on thumbnail for full-sized image.](#)

Fig. 9. Temperatures in the western trough averaged over the bottom two levels of the 21-level model for the cases of blocked channels, single-width diffusive channels, double-width diffusive channels, semiadvective channels, and (double-width) advective channels. The channel treatment in each case is indicated by the dash pattern. Heavy curves are for level 12, light curves for level 11.



[Click on thumbnail for full-sized image.](#)

Fig. 10. Abyssal temperatures in the western trough using vertical diffusivity enhanced above each opening to various levels ( $K_H$  in units of  $\text{cm}^2 \text{s}^{-1}$ ). Heavy curves are for level 12, light curves for level 11.



[Click on thumbnail for full-sized image.](#)

Fig. 11. Abyssal temperatures in the western trough using bottom drag coefficients of 0, 10, 30, and  $60 \text{ cm s}^{-1}$ , and an effectively infinite drag (no flow) at only the grid cells lying across each advective opening. The temperatures for the case of semiadvective openings are also shown. Heavy curves are for level 12, light curves for level 11.

Corresponding author address: Mr. Ross J. Murray, School of Earth Sciences, University of Melbourne, Parkville, Victoria 3052, Australia.  
E-mail: [rjmury@met.unimelb.edu.au](mailto:rjmury@met.unimelb.edu.au)

[top ▲](#)



